

Direct-Ink-Writing of Electroactive Polymers for Sensing and Energy Storage Applications

Rafael S. Pinto, João P. Serra, João C. Barbosa, Renato Gonçalves, Maria M. Silva, Senentxu Lanceros-Méndez,* and Carlos M. Costa*

Considering the high levels of materials used in the fields of electronics and energy storage systems, it is increasingly necessary to take into consideration environmental impact. Thus, it is important to develop devices based on environmentally friendlier materials and/or processes, such as additive manufacturing techniques. In this work, poly(vinylidene fluoride) (PVDF) and poly(vinylidene fluoride-co-hexafluoropropylene) (PVDF-HFP) are prepared by direct-ink-writing (DIW) by varying solvent evaporation temperature and fill density percentage. Different morphologies for both polymers are obtained, including dense films and porous membranes, as well as different electroactive β -phase content, thermal and mechanical properties. The dielectric constant and piezoelectric d_{33} coefficient for dense films reaches up to 16 at 1 kHz and 4 pC N^{-1} , respectively for PVDF-HFP with a fill density of 80 and a solvent evaporation temperature of 50°C . Porous structures are developed for battery separator membranes in lithium-ion batteries, with a highest ionic conductivity value of 3.8 mS cm^{-1} for the PVDF-HFP sample prepared with a fill density of 100 and a solvent evaporation temperature of 25°C , the sample showing an excellent cycling performance. It is demonstrated that electroactive films and membranes can be prepared by direct-ink writing suitable for sensors/actuators and energy storage systems.

1. Introduction

The interest in portable smart devices for monitoring sensors and communication has strongly increased in recent years. The corresponding increases in materials use and energy consumption is leading to large environmental impacts. Thus, research is focusing on environmentally friendlier materials and renewable energy systems in order to reduce the dependence on fossil fuels, avoiding environmental impacts, and without harming the increased demand for energy.^[1]

In particular, the Internet of Things paradigm demands the interconnection and powering of smart objects with improved integration and advanced functionalities.^[2] Novel approaches are thus also needed for the development of miniaturized, lightweight, flexible, and multi-shaped wearable devices. In order to achieve this type of structures, the manufacturing techniques have to be improved.

One of the promising technologies to be used in Additive Manufacturing (AM), that enables the fabrication of components with the characteristics mentioned above.^[3] AM is a 2D or 3D solid objects fabrication process, where the objects are fabricated layer by layer.^[4] This technology allows to convert digital data into physical object and opens new possibilities in the manufacturing industry, enabling the efficient fabrication of products from pre-defined files, with larger freedom of design and important environmental benefits. Unlike traditional object creation, that uses subtracting processes using cut or perforation methods to reach the desired object, AM represented an additive layer by layer process. The American Society for Testing and Materials (ASTM) defined seven AM categories: Binder jetting, Vat photo-polymerization, Sheet lamination, Powder bed fusion, Directed energy deposition, Material extrusion, and Material jetting.^[5]

Direct-ink-writing (DIW) technique is based on the extrusion of inks, inks formulation, and rheological behavior having a critical role in the printability of the materials. It presents interesting characteristics such as high resolution, arbitrary, and complex geometries, printability of multi-material types, low waste, and low cost.^[6]

This technique is being applied intensively in the area of batteries, mainly for the development of cathode and anode electrodes

R. S. Pinto, J. P. Serra, J. C. Barbosa, C. M. Costa
Centre of Physics

University of Minho
Braga 4710-053, Portugal
E-mail: cmscosta@fisica.uminho.pt

R. S. Pinto, J. P. Serra, C. M. Costa
Institute of Science and Innovation for Bio-Sustainability (IB-S)
University of Minho
Portugal

R. Gonçalves, M. M. Silva
Centre of Chemistry
University of Minho
Braga 4710-057, Portugal

S. Lanceros-Méndez
BCMaterials, Basque Center for Materials
Applications and Nanostructures
UPV/EHU Science Park, Leioa 48940, Spain
E-mail: senentxu.lanceros@bcmaterials.net

S. Lanceros-Méndez
IKERBASQUE
Basque Foundation for Science
Bilbao 48009, Spain

DOI: 10.1002/mame.202100372

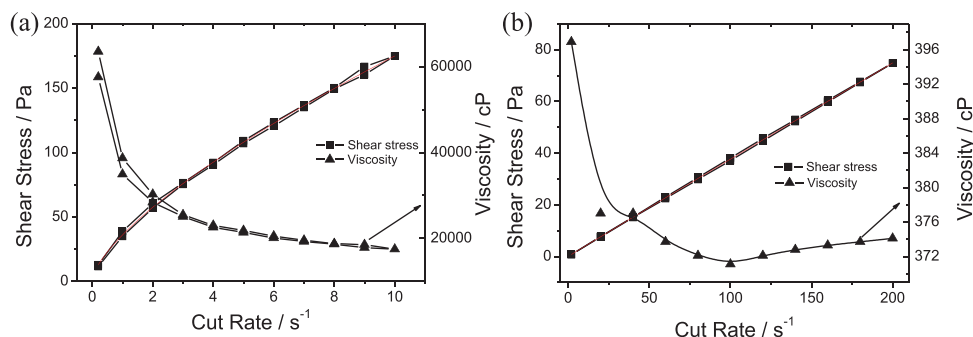


Figure 1. Shear stress and viscosity curves for a) PVDF and b) PVDF-HFP solutions.

based on LFP, LTO (cathodes), or graphene (anodes), among others, the printability of the separator membrane by DIW being scarcely explored.^[7]

In the case of sensors, different polymers such as wax or poly(carboxylic acid) have been used alone or with different fillers, including SiO₂, Na₂O, or CNT.^[6a]

One of the most used materials for sensors and actuators is piezoelectric ones.^[8]

The most used piezoelectric polymer is PVDF, a semi-crystalline fluorinated polymer composed by CH₂-CF₂ monomers.^[9] PVDF presents a large dielectric constant (6–12) and high electroactive response, including piezoelectric, pyroelectric, and ferroelectric effects.^[10] This polymer can crystallize in different phases, each with different chain conformations (α , β , γ , and δ). Of these phases, the β phase is the one with the largest polarization for unit cell and piezoelectric response.^[10] PVDF-HFP is a co-polymer of PVDF that presents a good resistance to solvents, thermoxidative degradation, and an exceptional hydrophobic stability. Like PVDF, this co-polymer shows the same crystalline phases. PVDF-HFP presents an amorphous phase (HFP) and a semicrystalline phase (PVDF), which gives it plasticity properties.^[10]

In recent years, it was verified an increasing scientific work that shows the characteristics and potentialities of the PVDF polymer and their co-polymers. These polymers have properties and characteristics that can enhance the performance of both batteries and sensors. Also, this polymer and its co-polymers are a material that is easily operated and can be adapted to various techniques.^[11] Printing techniques as manufacturing process of PVDF and co-polymers have been increasingly used due to their advantages face to the conventional techniques as well the polymer applicability.^[12]

PVDF and copolymer have been also explored for battery applications, in particular as polymer binder in anodes and cathodes^[13] and separator membranes.^[14] For separator membranes, the polymer has to be processed in a porous microstructure with good wettability and excellent thermal and mechanical properties.

In this context, the goal of this work is to process polymer solutions based on PVDF and PVDF-HFP by DIW technique, by varying solvent evaporation temperature and fill density percentage and correlate these processing parameters with the morphology, polymer phase, thermal and mechanical properties. Both dense and porous films have been produced for sensors/actuators and battery separator applications, respectively.

Table 1. Yield limit (τ_y), consistency index (K), and fluid behavior index (n) values obtained through the fitting of the data represented in Figure 1 with the Herschel–Bulkley equation.

	τ_y [Pa]	K	n
PVDF	2.01 ± 0.39	33.9 ± 1.7	0.71 ± 0.02
PVDF-HFP	0.01 ± 0.005	0.39 ± 0.02	0.99 ± 0.01

2. Results and Discussion

2.1. Rheological Evaluation

The rheological properties of the solutions were evaluated to tune printability. **Figure 1** presents the shear stress and viscosity as a function of shear rate for PVDF (**Figure 1a**) and PVDF-HFP (**Figure 1b**) solutions prepared after the same formulation procedure. It is to notice that the cut-off rate for both solutions is different since they have different viscosities and the appropriate torque has to be adjusted taking into account that both polymers have different molecular weights. **Figure 1** shows that the stress and viscosity values obtained increase and decrease, respectively, with increasing cut rates.

It should be noted that both solutions have a non-thixotropic behavior where the shear stress increases with increasing shear rate.^[15] The experimental data can be described by the Herschel–Bulkley law^[16] that describes the materials with a minimum yield stress. The red line in **Figure 1** shows the fitting to the experimental data and **Table 1** shows the minimum yield stress values, consistency index, and fluid behavior index obtained through the Herschel–Bulkley law.

For both solutions, the fluid index value is lower than 1 which allows to classify them as non-Newtonian and pseudo plastic.^[17] The minimum yield stress is different in both solutions, being lower for the solution with PVDF-HFP, since this polymer is characterized by a lower molecular weight compared to PVDF. The observed rheological behavior for both solutions is compatible with their processability by doctor blade and DIW.^[18]

2.2. Morphological Characteristics

Solutions were printed taking into account their rheological behavior. The morphology was obtained in surface and cross-section and the SEM images are shown in **Figures 2** and **3**,

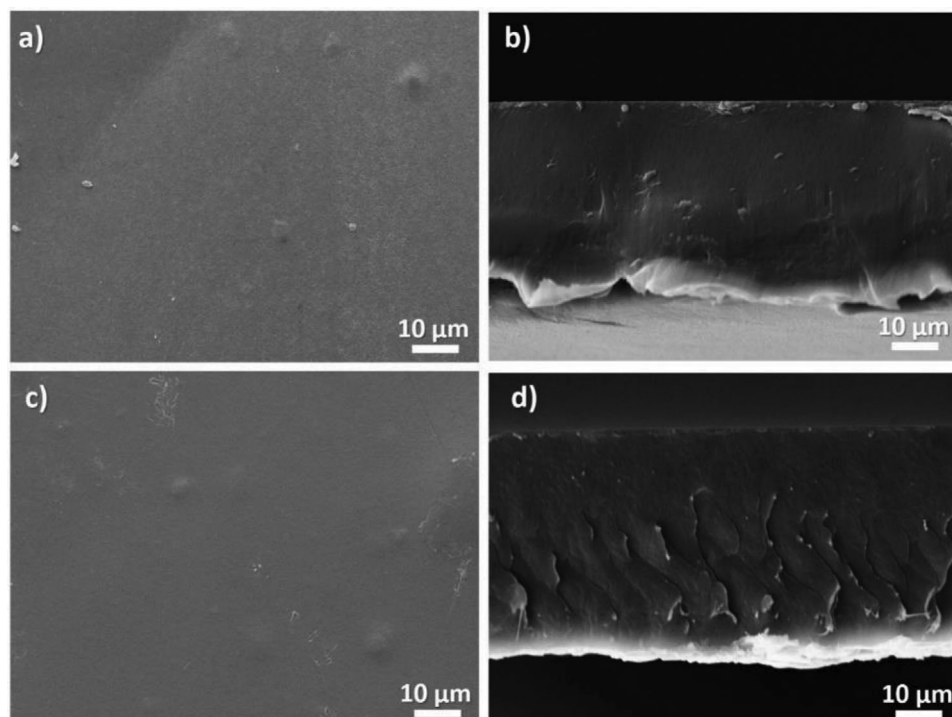


Figure 2. Surface (left) and cross-section (right) SEM images of the PVDF samples prepared after solvent evaporation at a–b) 25 and c–d) at 50 °C, printed with a fill density of 60%.

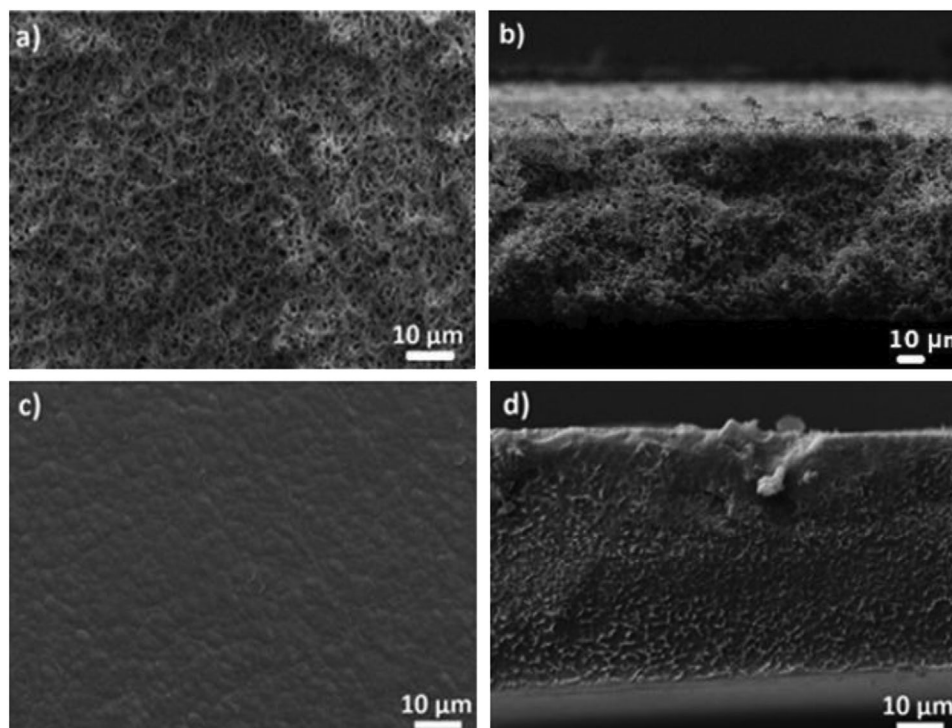


Figure 3. Surface (left) and cross-section (right) SEM images of the PVDF-HFP samples prepared after solvent evaporation at a–b) 25 and at c–d) 50 °C and printed with a fill density of 60%.

by varying the polymer processing temperature and fill density. Printed PVDF samples prepared after solvent evaporation temperature at 25 °C (Figure 2a,b) and 50 °C (Figure 2c,d) with a fill density of 60% show a compact microstructure without the presence of pores.

The observed morphology is correlated with the PVDF high molecular weight (92 840–1367 kDa) and melt viscosity (47–53 kp),^[19] that translates into an increase in the viscosity of the solution and an increase in the kinetic evaporation, preventing the phase separation process needed for obtaining the porous microstructure.^[20] Thus, PVDF can be processed in the form of dense films at room temperature by DIW.

Figure 3 shows the SEM images of the printed PVDF-HFP samples prepared after solvent evaporation at 25 °C (Figure 3a,b) and 50 °C (Figure 3c,d) with a fill density of 60%.

Samples prepared after solvent evaporation at 25 °C (Figure 3a,b) show high porosity with interconnected pores with size between 1 and 5 μm , both on the surface and in the cross-section of the sample. In this case, due to the slow solvent evaporation and low polymer viscosity (22–27 kp) and molecular weight,^[21] the formation of porosity is observed due to a liquid-liquid phase separation process^[20] and to the reduced mobility of the polymer chains preventing them to occupy the space left by the solvent during evaporation.^[20]

Similar porous morphology is also shown for the other fill densities of 80% and 100% (Figure S2, Supporting Information), the fill densities not affecting the microstructure of the samples.

For a solvent evaporation temperature of 50 °C (Figure 3c,d) a dense microstructure is obtained with a presence of well-defined spherulites. For solvent evaporation at this temperature, the polymer chains have mobility and occupy the free space left by the solvent after evaporation. This fact can also be observed for the other fill densities (80% and 100%) used in this work (Figure S2, Supporting Information).

The effect of printing fill density (Figure S1, Supporting Information) also shows correlation with the thickness of the samples, an increase of films thickness from 100 to 180 μm being observed for PVDF-HFP prepared with 60% to 100% fill density and 25 °C solvent evaporation temperature and from 30 to 60 μm for 60% to 100% fill density for samples prepared after solvent evaporation at 50 °C. These results are related to the fact that increasing fill density leads to a larger amount of solution being printed in the same printing area, leading to an increase in thickness. In the case of PVDF, this behavior is similar to that observed for PVDF-HFP.

2.3. Polymer Phase, Thermal, and Mechanical Properties and Surface Contact Angle

The vibrational spectrum of the samples allows to identify and quantify the polymeric phases present in the samples. PVDF and PVDF-HFP vibrational spectra are shown in Figure 4a for the samples prepared with different solvent evaporation temperature and fill density. The electroactive β phase content was quantified after Equation (2) and presented in Figure 4b. The infrared spectra show a similar band structure for all samples with characteristic peaks corresponding to the α (766 and 796 cm^{-1}) and β phases (840 cm^{-1}).^[10,22]

By comparing the electroactive phase content of both polymers processed at 60% fill density and the same solvent evaporation temperature (Figure 4b), it is observed that the polymer structure does not influence the amount of β phase obtained at low temperature of 25 °C but it does when the solvent evaporation temperature is higher (50 °C). At 50 °C and due to the higher solution viscosity from PVDF when compared to PVDF-HFP, the increased PVDF-HFP chain mobility leads to a larger β phase content.^[23]

In the case of PVDF-HFP, the solvent evaporation temperature also influences the β phase content, the samples evaporated to the lower temperature showing a larger β phase. At the solvent evaporation of 25 °C, the β phase content is independent of the fill density, remaining around 68% for all samples. For the solvent evaporation temperature of 50 °C, on the other hand, the β phase content of PVDF-HFP increases with increasing fill density mainly based on a geometrical effect due to the increasing sample thickness: whereas α phase crystallizes in the sample core, larger amount of β phase are formed at the surface as there is not enough time for nucleation of the more thermodynamically stable phase (α -phase).^[24] The influence of solvent evaporation temperature on the electroactive phase content of PVDF-HFP is in agreement with the literature.^[25]

With respect to the thermal characteristics, Figure 4c shows the DSC thermograms for PVDF and PVDF-HFP samples with 60% fill density and 25 and 50 °C solvent evaporation temperatures. It is verified that the fill density does not influence the thermal behavior of the PVDF-HFP samples, showing similar results (Figure S3, Supporting Information). For both polymeric matrices and regardless of the solvent evaporation temperature, during the heating process between 40 and 200 °C, an endothermic peak is observed related to the melting temperature of the crystalline phase of the polymer. The endothermic peak of PVDF is around 167 °C and for PVDF-HFP around 140 °C, both results are in agreement with the literature.^[26] Through the area of the melting peak, the degree of crystallinity, ΔX , of the samples has been calculated after Equation (3). The degree of crystallinity of PVDF and PVDF-HFP is 50% and 25%, respectively, independently of the fill density and solvent evaporation temperature. Figure 4c also shows that the cooling scan presents an exothermic peak, relative to the crystallization temperature of the polymers. The crystallization temperature value is 138 °C for PVDF and 108 °C for PVDF-HFP, regardless of the fill density and solvent evaporation temperature, also in agreement with the literature.^[26]

The thermal stability of the samples was evaluated by the TGA and results are shown in Figure 4d. Figure 4d shows the results for both PVDF and PVDF-HFP prepared at the solvent evaporation temperatures of 25 and 50 °C and a fill density of 60%. Regardless of the polymeric matrix and solvent evaporation temperature, a single thermal degradation step is observed for the samples, remaining stable up to 400 °C. The thermal degradation between 400 and 500 °C is associated with the decomposition of the $-\text{CH}_2-\text{CF}_2-$ groups of the polymers.^[27] The onset temperature is around 450 °C for all the samples, independently of polymer matrix, fill densities, and solvent evaporation temperature (see also Figure S4, Supporting Information).

The influence of the polymer matrix, solvent evaporation temperature and fill density on the sample mechanical characteristics are presented in the stress-strain curves of Figure 4e. All samples

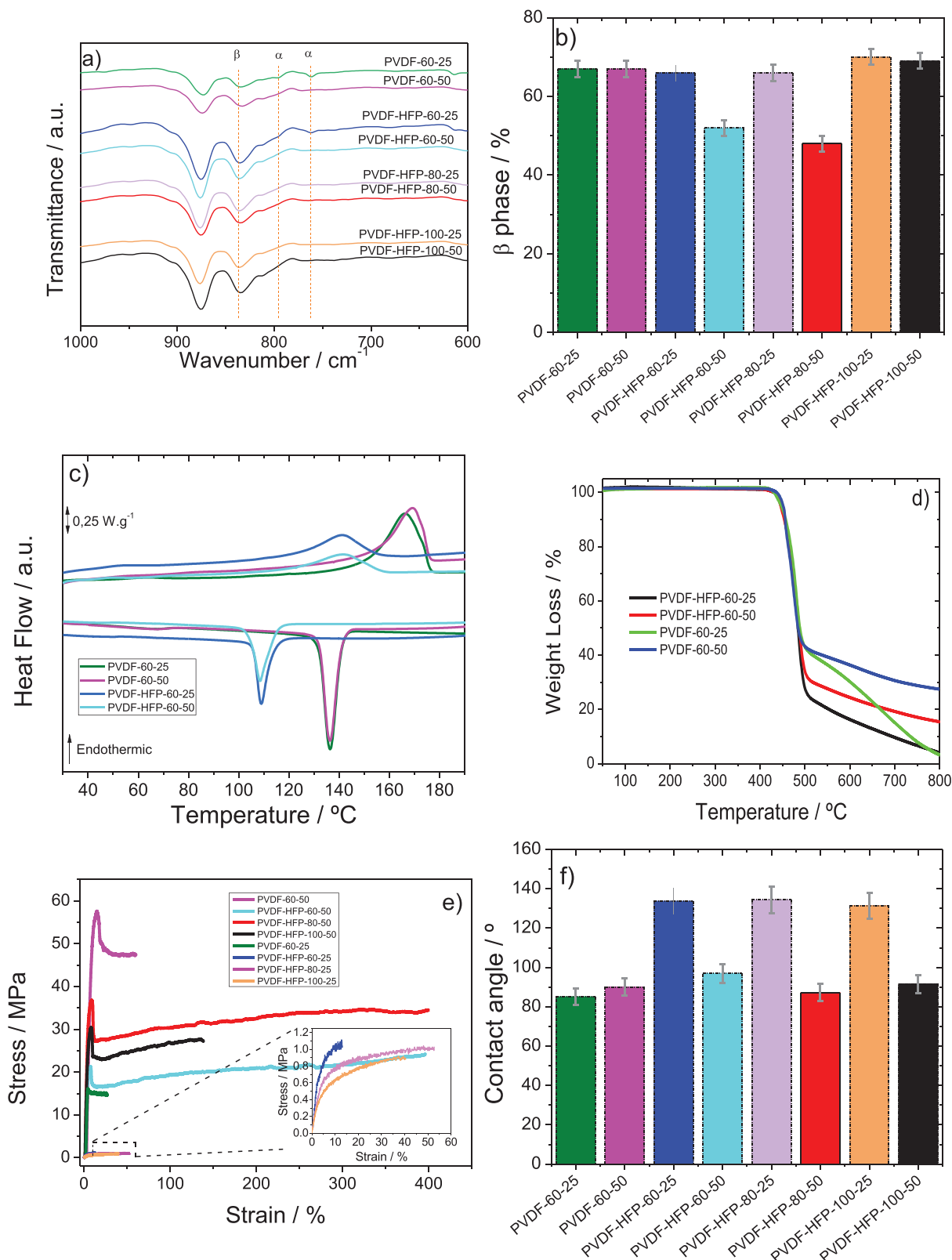


Figure 4. a) FTIR spectra for PVDF and PVDF-HFP samples obtained by DIW with different fill densities and solvent evaporation temperature of 25 and 50 $^{\circ}\text{C}$. b) Electroactive β phase content present in the samples. c) DSC thermograms of the PVDF and PVDF-HFP samples produced with 60% fill density and solvent evaporation temperature of 25 and 50 $^{\circ}\text{C}$. d) TGA thermograms of the same samples. e) Stress-strain curves and f) contact angle for all prepared samples.

Table 2. Young's Modulus and yield stress and strain for the different PVDF and PVDF-HFP samples.

Sample	Morphology	Young's modulus/ MPa \pm 5%	Yield stress/ MPa \pm 5%	Yield strain/ % \pm 5%
PVDF -60-25	Film	600	15.0	4.0
PVDF -60-50	Film	600	58.0	15.0
PVDF-HFP-60-25	Porous membrane	10	1.1	3.4
PVDF-HFP-60-50	Film	500	21.0	6.3
PVDF-HFP-80-25	Porous membrane	10	1.0	3.0
PVDF-HFP-80-50	Film	800	36.0	8.5
PVDF-HFP-100-25	Porous membrane	10	0.9	2.6
PVDF-HFP-100-50	Film	500	32.0	8.0

show the typical thermoplastic behavior, where two well-defined regions are detected, the elastic and plastic regimes.^[28] The solvent evaporation temperature has a significant effect on the mechanical properties as a consequence of the varying microstructure. The samples can be divided into two groups in relation to the stress-strain characteristics: the samples that present a dense film and porous membrane morphology. Samples with dense film morphology present higher Young modulus and yield stress and strain compared to the porous membranes once porosity induces a decrease in the mechanical properties. Also comparing the polymeric matrices, it is observed that PVDF shows a higher elasticity, related to the higher degree of crystallinity. The addition of the HFP monomer to the PVDF monomer decreases the mechanical properties due to the larger amorphous phase content. From the stress-strain curves, the values of Young's Modulus (determined at 3% of maximum elongation in the elastic region by the tangent method) and yield stress and strain have been determined, as presented in **Table 2**.

Both PVDF samples show high Young's Modulus (600 MPa), although the samples obtained after solvent evaporation temperature of 25 °C retain lower yield stress (15.0 MPa) and strain (4%) compared with the sample evaporated at 50 °C, probably due to microdefects created during the evaporation process, as well as to variations in the microstructure. The porous structure of the PVDF-HFP samples prepared at 25 °C shows a lower Young's Modulus and yield stress compared with the samples obtained at 50 °C, due to the HFP monomer which decreases the degree of crystallinity. In PVDF-HFP, higher fill densities in the fabrication process lead to an increase in the yield stress and Young's Modulus, the highest yield stress (36.0 MPa) and Young's Modulus (800 MPa) being obtained for the 80% fill density. The slight decrease of these properties for the fill density of 100% can be associated with microdefects created during its fabrication. These results demonstrate that DIW allows to suitably control the mechanical properties of the samples.

The contact angle results with ultrapure water are shown in Figure 4f, confirming the influence of sample morphology on the contact angle, the porous membranes showing higher values (130°) when compared with the dense films (90°). Further, PVDF-HFP also shows higher hydrophobicity when compared with PVDF, as the HFP groups increase the fluorine content and the hydrophobic character of the samples (see samples prepared at 25 °C). For the other samples, the contact angle is, approximately, 90° associated with its flat morphology and verifying a

hydrophobic character independently of the polymer type and fill density. The wettability was also evaluated for porous membranes with the electrolyte solution (EC:DMC, 1:1 vol., 1 M LiPF₆), showing a contact angle of 0° for all samples, once the electrolyte solution was immediately absorbed by the samples and confirming the high affinity between the polymers and the electrolyte solution due to interaction between the polymer chains with the linear alkyl carbonates.^[29]

2.4. Dielectric Constant and Piezoelectric Coefficient

The samples obtained in the form of dense films, PVDF and PVDF-HFP samples prepared after solvent evaporation at 50 °C, were subjected to dielectric measurements due to their applicability as sensors and actuators.^[30] **Figure 5a** shows the real part of the dielectric constant and **Figure 5b** the corresponding dielectric losses.

Figure 5a shows that the real part of the electric function, ϵ' , has a similar frequency response for all samples, the dielectric constant decreasing with increasing frequency due to the accumulation of charge carriers at the electrode-sample (Maxwell–Wagner–Sillars effect) and also the limited dipolar mobility with increasing frequency.^[31]

PVDF-HFP-80-50 shows the highest dielectric constant (16 at 1 kHz), followed by PVDF-HFP-60-50. It is verified that β phase contents, degree of crystallinity, and mechanical characteristics affect the dielectric constant, due to the PVDF molecule polarization effect.^[32] This behavior is mainly related to the cooperative orientational movement of the existing dipoles in the crystalline-amorphous interphase of PVDF.^[33]

In relation to the dielectric losses, the behavior is practically similar for all samples, the $\tan \delta$ increasing with increasing frequency in the high-frequency region, which is attributed to the confined mobility and the α_a relaxation process, that is, micro-Brownian movement of the amorphous phase chain segments or movement of crystalline-amorphous interphase chain segments.^[34] **Table 3** shows the dielectric response of PVDF and PVDF-HFP at different fill densities.

The obtained dielectric constant for PVDF is in agreement with the values typically obtained in PVDF after processing by doctor blade technique.^[35] Moreover, for PVDF-HFP (fill density of 60% and 80%) the obtained dielectric constant result is higher than the ones verified in the literature (10 at 1 kHz at 100 °C)

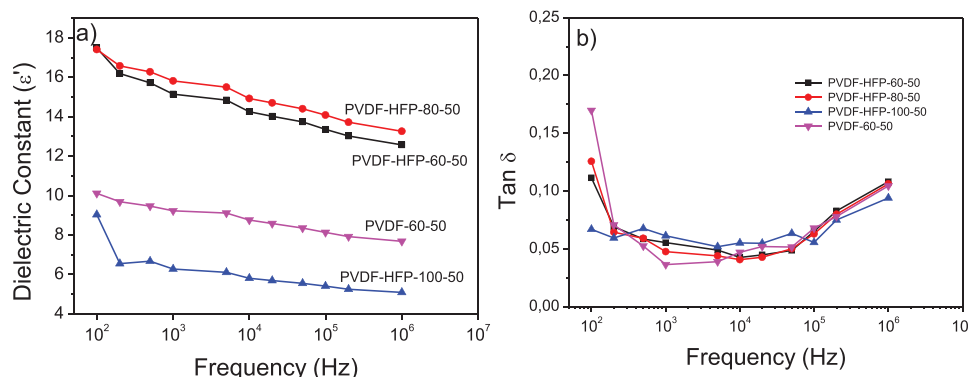


Figure 5. a) Dielectric constant and b) dielectric losses of PVDF and PVDF-HFP samples prepared after solvent evaporation at 50 °C.

Table 3. Values of Dielectric Constant and Dielectric loss at 1 kHz frequency.

Samples	Frequency [1 kHz]	
	Dielectric constant	Dielectric loss
PVDF-HFP-60-50	15	0.05
PVDF-HFP-80-50	16	0.05
PVDF-HFP-100-50	6	0.06
PVDF-60-50	9	0.04

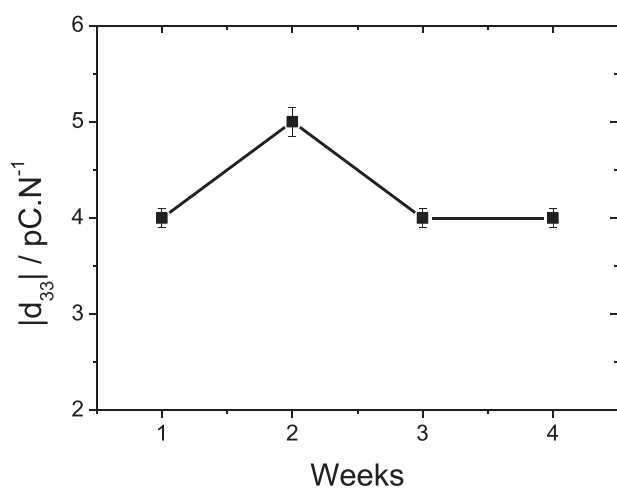


Figure 6. Variation of the modulus of the piezoelectric coefficient for PVDF-HFP-80-50 as a function of time.

for samples obtained by doctor blade technique, the processing technique, and conditions also affecting the β -phase content and the degree of crystallinity.^[36] Thus, it is proven that the direct-ink-printed films show suitable characteristics for being implemented in sensor and actuator applications, as often explores for PVDF films in the electroactive phase.^[37]

The suitability of the printed samples for piezoelectric sensor applications, the PVDF-HFP-80-50 sample was poled and the piezoelectric coefficient is presented in **Figure 6** as a function of time, to show the stability of the response. The results are repre-

sentative, within variations of the piezoelectric response, for the rest of the dense films.

It is observed that the modulus of the piezoelectric coefficient is stable after 4 weeks with variation between 4 and 5 pC N⁻¹ for the printed sample, the value being in agreement with the literature for this polymer ($|d_{33}| \approx 6\text{--}12$ pC N⁻¹).^[36] This value is dependent on the degree of crystallinity and is suitable for sensor applications.

2.5. Uptake, Ionic Conductivity, and Electrochemical Tests

The fact that the PVDF-HFP samples prepared after solvent evaporation at 25 °C exhibit a porous morphology, indicate their suitability for battery separator applications.^[11b] The effect of fill density percentage on the electrolyte absorption, ionic conductivity, and battery cycling stability were studied.

The capability of the membranes to uptake the electrolyte solution is shown in **Figure 7a** as a function of time. It is shown that the absorption of the electrolyte solution occurs very fast and it is not dependent on the fill density percentage, being observed an increase in weight larger than 300% after 15 s for all samples. The observed effect is a result of the interaction of the organic solvents (EC and DMC) and the polar functional groups of PVDF-HFP, where the electrolyte stays lodged in the amorphous phase of the polymer.^[38]

The ionic conductivity of the PVDF-HFP porous membrane samples was determined through impedance spectroscopy tests. **Figure 7b** shows the Nyquist plots for each sample, the electrical behavior being characterized by a straight line in all frequency range, resulting from ionic conduction. From the Nyquist plot, it is possible to calculate the ionic conductivity of the samples, by using Equation (5). The results, **Table 4**, indicate that regardless of the fill density, the ionic conductivity is above 10⁻³ S cm⁻¹, thus confirming the possibility of being applied as battery separator membranes.^[39] The observed differences in the ionic conductivity are associated with the slight differences in the porous morphologies of the membranes.

To evaluate the effect of PVDF-HFP porous membranes prepared with different fill densities on battery performance, C-LiFePO₄ cathodic half-cells were fabricated and the cyclic performance obtained at applied rates between C/8 and 2C. **Figure 7c** shows a typical charge-discharge profile for the fifth

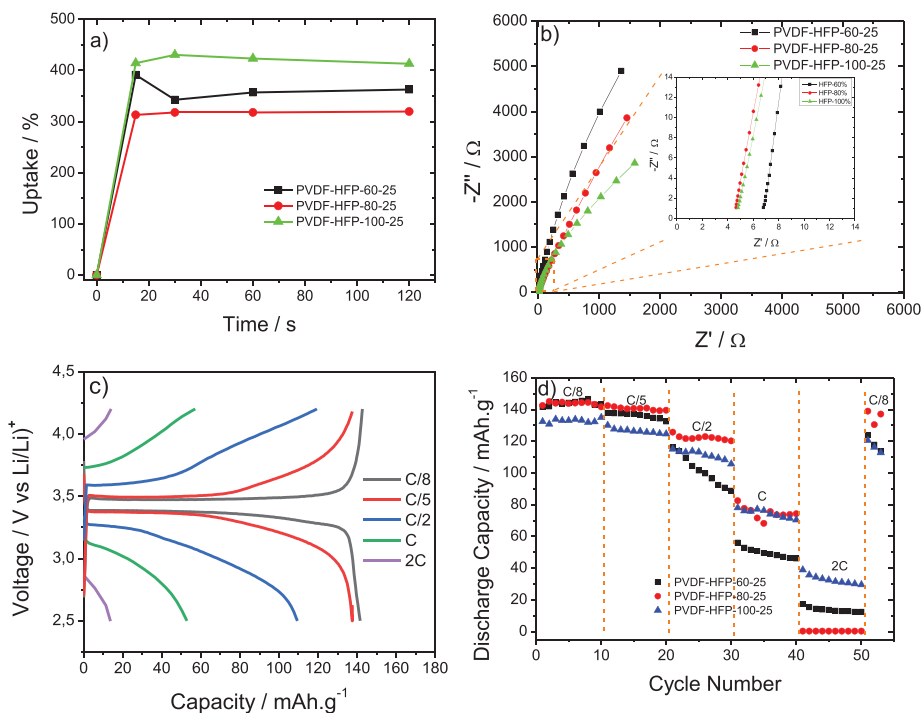


Figure 7. a) Uptake percentage value of the electrolyte solution over as a function of time, b) Nyquist plot c) 5th charge-discharge half-cell cycle profiles at rates from C/8 to 2C and d) discharge capacity for the porous PVDF-HFP samples produced for the various fill densities percentages.

Table 4. Ionic conductivity of the PVDF-HFP porous membrane prepared with different fill densities.

Samples	Ionic conductivity [$\text{mS cm}^{-1} \pm 5\%$]
PVDF-HFP-60-25	1.4 ± 0.1
PVDF-HFP-80-25	3.7 ± 0.2
PVDF-HFP-100-25	3.8 ± 0.2

cycle from C/8 to 2C rates for the PVDF-HFP porous membranes with 60% of fill density. The charge–discharge profile is representative for the other PVDF-HFP porous membranes, independently of the fill density. Across the shifting between the different applied rates, the battery suffers influence from ionic transport on the ohmic polarization and interfacial reaction resistance on the lithium electrode, leading to a decrease in battery capacity with increasing C rate.^[40] Regardless of the applied rate, Figure 7c presents a typical C-LiFePO₄ cathode profile that reflects the disinsertion of lithium in the charging process and the insertion of lithium in the discharge process corresponding to the Fe²⁺/Fe³⁺ process and this behavior is regardless of the sample and cycle number.^[40]

Figure 7d shows the discharge capacity values for all C rates as a function of the cycle number, for the half-cells prepared with the PVDF-HFP porous membranes prepared with different fill densities. The discharge capacity remains stable along the cycle number. Further, the discharge capacity from the recovery rate at the end of the C rate demonstrates the high performance of the samples. It can be seen that, for low applied current rates (C/8), the capacity value between the various samples

is very similar. By increasing C rate above C/5, differences in the discharge capacity can be observed among the different membranes, resulting mainly from the different values of ionic conductivity of each sample. High cyclic performance is observed in the sample with 100% fill density due to its high ionic conductivity, high uptake percentage capacity, and also its porous morphology. For this sample and applying a 2 C rate, the battery achieved a discharge capacity of 38 mAh g⁻¹ which demonstrates its excellent cyclic performance. PVDF-HFP-80-25 and PVDF-HFP-60-25 show discharge capacities of 1 and 13 mAh g⁻¹, respectively.

It is no notice that the electrochemical behavior is improved with respect to the one reported in the literature for PVDF-HFP 5/95 produced by doctor blade technique in Li/LiFePO₄ cells, which shows a discharge capacity of 0.05 mAh g⁻¹ at 2 C.^[41]

Overall, it is shown that the porous PVDF-HFP samples with 100% fill density obtained through DIW show good electrochemical performance and they can be used as battery separators in the next generation of lithium-ion batteries. Also, it has been proven that DIW allows to tune separator morphology and physical-chemical characteristics.

3. Conclusion

Printed samples of poly(vinylidene fluoride) (PVDF) and poly(vinylidene fluoride-co-hexafluoropropylene) (PVDF-HFP) samples were prepared by 3D Dir DIW by varying solvent evaporation temperature and fill density. Dense films and porous membranes were obtained, suitable for sensors/actuators and lithium-ion battery separator applications, respectively. The different morphologies are obtained by varying processing

parameters, including processing temperature, that allow producing porous and dense morphologies. Further, there is a correlation between print fill density and sample thickness. The β -phase, thermal and mechanical properties for both polymers can be controlled through the solvent evaporation temperature and fill density. Regarding the electroactive β phase content of the samples, it is not affected by the fill density for solvent evaporation at 25 °C but increases with fill density for processing temperatures of 50 °C. On the other hand, the degree of crystallinity of the printed PVDF and PVDF-HFP samplers is independent of fill density and solvent evaporation temperature.

The sample with the highest dielectric constant ($\epsilon' = 16$ at 1 kHz) was obtained for the PVDF-HFP film prepared with a fill density of 80% and processed at 50 °C. This sample also shows a piezoelectric coefficient of $|d_{33}| = 4$ pC N⁻¹. For porous membranes, the highest ionic conductivity value (3.8 mS cm⁻¹) is obtained for PVDF-HFP prepared with a fill density of 100% and processed at 25 °C.

Thus, it is demonstrated that the obtained PVDF and PVDF-HFP samples, processable by DIW technique, show adequate thermal and mechanical properties for the AM development of sensors/actuators and battery separator applications.

4. Experimental Section

Materials: Poly(vinylidene fluoride)—PVDF (Kynar PVDF HSV900) and poly(vinylidene fluoride-co-hexafluoropropylene)—PVDF-HFP (Kynarflex PVDF-HFP 2801-00107) were purchased from Arkema. *N,N*-dimethylformamide—DMF, 99% purity, and *N*-methyl-2-pyrrolidone—NMP, 99%, were obtained from Panreac applichem and Merck, respectively. C-LiFePO₄ (C-LFP) was obtained from Phostech Lithium. Carbon black particles (Super P-C45) were obtained from Timcal Graphite & Carbon. PVDF (Kynar PVDF HSV1800) was purchased from Arkema and was used as polymer binder in batteries. The electrolyte solution for battery applications, lithium hexafluorophosphate (LiPF₆) salts in 1 M ethylene carbonate (EC)/dimethyl carbonate (DMC) 1/1 (vol./vol.) was obtained from Solvionic. All reagents and materials were used as received.

Sample Processing: Being not an environmentally friendly solvent, DMF was still the most used solvent for PVDF-related samples, and therefore it was used in the present investigation. Other solvents such as *N,N*-dimethylpropyleneurea (DMPU) and 1,3-dioxolane were being tested for the processing of fluorinated polymers to reduce processing environmental impact.^[42] Neat PVDF and PVDF-HFP films were prepared by dissolving the polymer in DMF (15/85 wt.%) under magnetic stirring at room temperature. After the polymer was completely dissolved, the solution was placed in a syringe with a needle diameter of 0.5 mm and then placed in a 3DCultures-Bioprinter. A circle pattern filled with zig-zag lines was used for the printing process (Figure S1, Supporting Information). After process optimization, bed and extruder temperature were set at 25 °C and the printing speed at 2 mm³ s⁻¹. The solution was printed on a glass substrate and then evaporated in an oven (JP selecta) at 25 or 50 °C for 1 h and 30 min. After this preparation procedure it was expected to obtain a porous polymer membrane (25 °C) or a homogenous non-porous polymer film (50 °C).^[11c,43] Further, fill density parameter from 60% to 100% were varied on the printed samples due to its influence on sample thickness (Figure S1, Supporting Information).

Characterization Techniques: The rheological properties of the solutions were determined in a Brookfield DV2T Touch Screen Viscometer using cone-plate geometry with a CPA-52Z cone (3° cone angle, 1.2 cm cone radius).

The flow curves were fitted to the Herschel–Bulkley model:^[44]

$$\sigma = \sigma_y + K\dot{\gamma}^n \quad (1)$$

where σ_y is the critical stress that delimits the fluid-like behavior of the paste, which flows with a power-law dependence in the shear rate, characterized by a thinning exponent n and a consistency index K .

For the morphology evaluation of the printed samples, the samples were first coated with a thin gold layer using a sputter coating (Polaron, model SC502) and then analyzed using a Scanning Electron Microscopy (SEM, Quanta 650, from FEI) with an accelerating voltage of 15 kV. Structural analysis was evaluated by Fourier Transform Infrared (FTIR) spectroscopy in the Attenuated Total Reflectance (ATR) mode. Measurements were performed with a Jasco FT/IR-6100 equipment at room temperature from 4000 to 600 cm⁻¹, using 64 scans at a resolution of 4 cm⁻¹. The electroactive β -phase content of the samples was obtained from the FTIR/ATR spectra using Equation (2):^[11c]

$$F(\beta) = \frac{A_{840}}{(K_{840}/K_{766})A_{766} + A_{840}} \quad (2)$$

where $F(\beta)$ represents the β -phase content; A_{840} and A_{766} are the absorbances at 840 and 766 cm⁻¹, corresponding to the β - and α -phase of the polymer, respectively; K_{840} and K_{766} are the absorption coefficients at the respective wave number with values of 7.7×10^4 and 6.1×10^4 cm² mol⁻¹, respectively.^[10] The contact angle of the samples was obtained with a Data physics Contact Angle System OCA20. For this purpose, a drop with 3 μ L of ultrapure water or electrolyte was deposited at the samples surface.

The thermal properties of the different samples were determined by Differential Scanning Calorimetry (DSC) and Thermal Gravimetric Analysis (TGA). DSC was performed in a Perkin Elmer DSC 8000 apparatus, at a heating rate of 10 °C min⁻¹, within a nitrogen atmosphere. Two thermograms were performed, one heating and one cooling, between 25 and 200 °C. The degree of crystallinity (ΔH_c) was calculated from the DSC scans, using Equation (3):^[10]

$$\Delta X_c = \frac{\Delta H}{x\Delta H_\alpha + y\Delta H_\beta} \quad (3)$$

where ΔH represents the sample melting enthalpy; x and y the α and β phase content (obtained from the FTIR analysis through Equation (1)); ΔH_α the melting enthalpy of PVDF α phase and ΔH_β the melting enthalpy of PVDF β phase, 93.07 and 103.4 J g⁻¹, respectively.^[10]

The TGA analysis was performed with a Perkin Elmer Pyris 1 TGA in the temperature range between 25 and 800 °C at a heating rate of 10 °C min⁻¹, under a nitrogen atmosphere flow.

The stress–strain mechanical measurements were carried out at room temperature with a TST350 tensile testing set up from Linkam Scientific Instruments at a strain rate of 15 μ m s⁻¹. Each sample was measured in triplicate.

Dielectric constant measurements were carried out with a Quadtech 1920 LCR precision meter. The measurements were performed at room temperature in a frequency range of 20 Hz to 1 MHz, applying a voltage of 0.5 V. Circular gold electrodes with 5 mm diameter were deposited by magnetron sputtering onto both sides of each sample through a Polaron SC502 apparatus to obtain a parallel plate capacitor geometry. The capacity and $\tan \delta$ were measured and the real part of the dielectric function (ϵ') was calculated taking into consideration the geometrical parameters of the capacitor.^[45]

After an optimization procedure, the dense films were poled through corona discharge within a home-made corona chamber with an applied voltage of 10 kV for 1 h at 120 °C at a constant distance of 2 cm between sample and tip. The piezoelectric coefficient, d_{33} , of the films were measured using a d_{33} meter APC YE2730A.

Electrolyte Uptake, Ionic Conductivity, Half-Cell Battery Assembly, and Characterization: The uptake percentage of the membranes was calculated after Equation (4):

$$\text{Uptake \%} = \frac{m - m_0}{m_0} \times 100 \quad (4)$$

where samples were first weighed (m_0), then immersed in an electrolyte solution (EC:DMC, 1:1 vol., 1 M LiPF₆) for 15 s, and weighed (m) again. This last step was repeated for 30, 60, and 120 s. The procedure allows to calculate the percentage of electrolyte solution absorbed by each sample.

Samples' ionic conductivity was determined using a constant volume support, equipped with gold blocking electrodes located within a Buchi TO 50 oven. Impedance measurements were carried out at frequencies between 500 mHz and 65 kHz using an Autolab PGSTAT-12 (Eco Chemie), at room temperature and the ionic conductivity (σ) was calculated by:

$$\sigma = \frac{t}{A \cdot R_b} \quad (5)$$

where t is the thickness, A is the area and R_b is the bulk resistivity of the sample, obtained by the interception of the imaginary impedance (minimum value of Z'') with the slanted line in the real impedance (Z').

Battery performance was obtained in Li/C-LFP half-cells. Swagelok type battery configuration was assembled in a homemade argon-filled glove-box, with all materials previously dried over night at 90 °C under vacuum. As anode, a metallic lithium disk (99.9% purity) with 8 mm diameter and 0.75 mm thickness was used. The cathode slurry was obtained with the proportions of 80 wt.% C-LiFePO₄, 10 wt.% carbon black, and 10 wt.% PVDF in NMP solvent. The cathode electrode slurry was casted on aluminum foil by doctor-blade technique and placed in an oven at 80 °C for 2 h, to ensure solvent evaporation.^[46] The selected samples used as separator membranes (10 mm diameter) were soaked in the electrolyte solution and placed between electrodes.

Galvanostatic charge/discharge cycles of the half-cells were obtained at room temperature using a Landt CT2001A instrument. The cycles were carried out in the voltage range from 2.5 to 4.2 V at current densities from C/8 to 2C (C = 170 mAh g⁻¹). Electrochemical Impedance Spectroscopy (EIS) was carried out using an Autolab PGSTAT12 instrument. The measurement frequency ranged from 0.5 MHz to 10 mHz with an amplitude of 10 mV.

Supporting Information

Supporting Information is available from the Wiley Online Library or from the author.

Acknowledgements

The authors thank the FCT (Fundação para a Ciência e Tecnologia) for financial support under the framework of Strategic Funding grants UID/CTM/50025/2021, UID/FIS/04650/2021, UID/EEA/04436/2021 and UID/QUI/0686/2021; and supported by FEDER funds through the COMPETE 2020 Programme under the project number PTDC/FIS-MAC/28157/2017 and POCI-01-0145-FEDER-007688. The authors also the grant SFRH/BD/140842/2018 (J.C.B.) and contracts under the Stimulus of Scientific Employment, Individual Support CEECIND/00833/2017 (R.G.) and Contract 2020.04028.CEECIND (C.M.C.). The authors thank funding by the Spanish State Research Agency (AEI) and the European Regional Development Fund (ERFD) through the project PID2019-106099RB-C43/AEI/10.13039/501100011033 and from the Basque Government under the ELKARTEK, HAZITEK, and PIBA (PIBA-2018-06) programs is also acknowledged.

Conflict of Interest

The authors declare no conflict of interest.

Data Availability Statement

Research data are not shared.

Keywords

additive manufacturing, lithium-ion batteries, poly(vinylidene fluoride), poly(vinylidene fluoride-co-hexafluoropropylene), sensors, separator membranes

Received: May 25, 2021

Revised: July 6, 2021

Published online: August 6, 2021

- [1] a) C. M. Costa, Y.-H. Lee, J.-H. Kim, S.-Y. Lee, S. Lanceros-Méndez, *Energy Storage Mater.* **2019**, 22, 346; b) C.-F. Du, Q. Liang, Y. Luo, Y. Zheng, Q. Yan, *J. Mater. Chem. A* **2017**, 5, 22442.
- [2] J. Oliveira, V. Correia, H. Castro, P. Martins, S. Lanceros-Mendez, *Addit. Manuf.* **2018**, 21, 269.
- [3] a) D. S. Ginley, D. Cahen, *Fundamentals of Materials for Energy and Environmental Sustainability*, Cambridge University Press, Cambridge, UK **2011**; b) S. Campanari, G. Manzolini, F. Garcia de la Iglesia, *J. Power Sources* **2009**, 186, 464.
- [4] H. Ragoes, S. Menkin, Y. Kamir, A. Gladkikh, T. Mukra, G. Kosa, D. Golodnitsky, *Sustainable Energy Fuels* **2018**, 2, 1542.
- [5] C. M. Costa, R. Gonçalves, S. Lanceros-Méndez, *Energy Storage Mater.* **2020**, 28, 216.
- [6] a) L. Hao, D. Tang, T. Sun, W. Xiong, Z. Feng, K. E. Evans, Y. Li, *International Journal of Precision Engineering and Manufacturing-Green Technology* **2021**, 8, 665; b) V. G. Rocha, E. Saiz, I. S. Tirichenko, E. García-Tuñón, *J. Mater. Chem. A* **2020**, 8, 15646.
- [7] S. Tagliaferri, A. Panagiotopoulos, C. Mattevi, *Mater. Adv.* **2021**, 2, 540.
- [8] C. Ribeiro, D. M. Correia, S. Ribeiro, M. M. Fernandes, S. Lanceros-Mendez, *MRS Adv.* **2018**, 3, 1671.
- [9] I. Abdullah, M. Yahaya, M. H. Jumali, H. Shanshool, *Surf. Rev. Lett.* **2015**, 23, 1650005.
- [10] P. Martins, A. C. Lopes, S. Lanceros-Mendez, *Prog. Polym. Sci.* **2014**, 39, 683.
- [11] a) G.-D. Kang, Y.-M. Cao, *J. Membr. Sci.* **2014**, 463, 145; b) J. C. Barbosa, J. P. Dias, S. Lanceros-Méndez, C. M. Costa, *Membranes* **2018**, 8, 45; c) C. Ribeiro, C. M. Costa, D. M. Correia, J. Nunes-Pereira, J. Oliveira, P. Martins, R. Gonçalves, V. F. Cardoso, S. Lanceros-Méndez, *Nat. Protoc.* **2018**, 13, 681.
- [12] a) L. Zeng, P. Li, Y. Yao, B. Niu, S. Niu, B. Xu, *Mater. Today Nano* **2020**, 12, 100094; b) M. Marandi, J. Tarbuton, *Procedia Manufacturing* **2019**, 34, 666.
- [13] A. Gören, C. M. Costa, M. M. Silva, S. Lanceros-Mendez, *Solid State Ionics* **2016**, 295, 57.
- [14] C. M. Costa, J. L. Gomez Ribelles, S. Lanceros-Méndez, G. B. Appetecchi, B. Scrosati, *J. Power Sources* **2014**, 245, 779.
- [15] C. M. Bui, T. X. Ho, *AIP Adv.* **2020**, 10, 035303.
- [16] W. H. Herschel, R. Bulkley, *Kolloid-Z.* **1926**, 39, 291.
- [17] D. V. Boger, *Nature* **1977**, 265, 126.
- [18] Z. Żółek-Tryznowska, in *Printing on Polymers* (Eds: J. Izdebska, S. Thomas), William Andrew Publishing, Norwich, NY **2016**, pp. 87–99.
- [19] M. Wang, J. Hu, Y. Wang, Y.-T. Cheng, *J. Electrochem. Soc.* **2019**, 166, A2151.
- [20] J. C. C. Ferreira, T. S. Monteiro, A. C. Lopes, C. M. Costa, M. M. Silva, A. V. Machado, S. Lanceros-Mendez, *J. Non-Cryst. Solids* **2015**, 412, 16.
- [21] R. Amin-Sanayei, W. He, in *Advanced Fluoride-Based Materials for Energy Conversion* (Eds: T. Nakajima, H. Groult), Elsevier, Amsterdam **2015**, pp. 225–235.
- [22] A. Biswas, K. Henkel, D. Schmeißer, D. Mandal, *Phase Transitions* **2017**, 90, 1205.

- [23] S. P. Muduli, S. Parida, S. K. Rout, S. Rajput, M. Kar, *Mater. Res. Express* **2019**, 6, 095306.
- [24] D. Yang, Y. Chen, *J. Mater. Sci. Lett.* **1987**, 6, 599.
- [25] L. Ruan, X. Yao, Y. Chang, L. Zhou, G. Qin, X. Zhang, *Polymers* **2018**, 10, 228.
- [26] a) B. Wang, H.-X. Huang, *Composites, Part A* **2014**, 66, 16; b) K. Polat, *Appl. Phys. A* **2020**, 126, 497.
- [27] R. Gonçalves, D. Miranda, A. M. Almeida, M. M. Silva, J. M. Meseguer-Dueñas, J. L. G. Ribelles, S. Lanceros-Méndez, C. M. Costa, *Sustainable Mater. Technol.* **2019**, 21, e00104.
- [28] a) P. Costa, J. Silva, V. Sencadas, C. M. Costa, F. W. J. Van Hattum, J. G. Rocha, S. Lanceros-Mendez, *Carbon* **2009**, 47, 2590; b) J. Vicente, P. Costa, S. Lanceros-Mendez, J. M. Abete, A. Iturrospe, *Materials* **2019**, 12, 3545.
- [29] S. W. Choi, J. R. Kim, Y. R. Ahn, S. M. Jo, E. J. Cairns, *Chem. Mater.* **2007**, 19, 104.
- [30] V. T. Rathod, D. R. Mahapatra, A. Jain, A. Gayathri, *Sens. Actuators, A* **2010**, 163, 164.
- [31] M. Samet, V. Levchenko, G. Boiteux, G. Seytre, A. Kallel, A. Serghei, *J. Chem. Phys.* **2015**, 142, 194703.
- [32] a) W. Xia, Z. Zhang, *IET Nanodielectrics* **2018**, 1, 17; b) R. Gregorio, Jr., E. M. Ueno, *J. Mater. Sci.* **1999**, 34, 4489.
- [33] a) B. Hahn, J. Wendorff, D. Y. Yoon, *Macromolecules* **1985**, 18, 718; b) Y. Ando, T. Hanada, K. Saitoh, *J. Polym. Sci., Part B: Polym. Phys.* **1994**, 32, 179.
- [34] H. Arisawa, O. Yano, Y. Wada, *Ferroelectrics* **1981**, 32, 39.
- [35] J. Gomes, J. Serrado Nunes, V. Sencadas, S. Lanceros-Mendez, *Smart Mater. Struct.* **2010**, 19, 065010.
- [36] R. E. Sousa, J. Nunes-Pereira, J. C. C. Ferreira, C. M. Costa, A. V. Machado, M. M. Silva, S. Lanceros-Mendez, *Polym. Test.* **2014**, 40, 245.
- [37] C. M. Costa, V. F. Cardoso, R. Brito-Pereira, P. Martins, D. M. Correia, V. Correia, C. Ribeiro, P. M. Martins, S. Lanceros-Méndez, in *Fascinating Fluoropolymers and Their Applications* (Eds: B. Ameduri, S. Fomin), Elsevier, Amsterdam **2020**.
- [38] X. Liang, D. Han, Y. Wang, L. Lan, J. Mao, *RSC Adv.* **2018**, 8, 40498.
- [39] Z. Lu, F. Sui, Y.-E. Miao, G. Liu, C. Li, W. Dong, J. Cui, T. Liu, J. Wu, C. Yang, *J. Energy Chem.* **2021**, 58, 170.
- [40] W. Xiao, L. Zhao, Y. Gong, S. Wang, J. Liu, C. Yan, *RSC Adv.* **2015**, 5, 34184.
- [41] R. E. Sousa, J. Nunes-Pereira, C. M. Costa, M. M. Silva, S. Lanceros-Méndez, J. Hassoun, B. Scrosati, G. B. Appetecchi, *J. Power Sources* **2014**, 263, 29.
- [42] a) S. Gonçalves, J. Serrado-Nunes, J. Oliveira, N. Pereira, L. Hilliou, C. M. Costa, S. Lanceros-Méndez, *ACS Appl. Electron. Mater.* **2019**, 1, 1678; b) J. Nunes-Pereira, P. Martins, V. F. Cardoso, C. M. Costa, S. Lanceros-Méndez, *Mater. Des.* **2016**, 104, 183.
- [43] J. P. Serra, R. S. Pinto, J. C. Barbosa, D. M. Correia, R. Gonçalves, M. M. Silva, S. Lanceros-Mendez, C. M. Costa, *Sustainable Mater. Technol.* **2020**, 25, e00176.
- [44] P. C. F. Møller, J. Mewis, D. Bonn, *Soft Matter* **2006**, 2, 274.
- [45] A. Schönhals, F. Kremer, in *Broadband Dielectric Spectroscopy*, (Eds: F. Kremer, A. Schönhals), Springer Berlin Heidelberg, Berlin, Heidelberg **2003** pp. 1–33.
- [46] R. Gonçalves, P. Sharma, P. Ram, S. Ferdov, M. M. Silva, C. M. Costa, R. Singhal, R. K. Sharma, S. Lanceros-Méndez, *J. Alloys Compd.* **2021**, 853, 157208.